WILEY | Hindawi

Research Article

UV-fs-LA-ICP-MS Analysis of CO$_2$-Rich Fluid Inclusions in a Frozen State: Example from the Dahu Au-Mo Deposit, Xiaoqinling Region, Central China

Wei Jian [iD],[1] Moritz Albrecht,[2] Bernd Lehmann,[3] Jingwen Mao,[1] Ingo Horn,[2] Yanhe Li,[1] Huishou Ye,[1] Zongyan Li,[4] Guanguan Fang,[4] and Yongsheng Xue[4]

[1]*MLR Key Laboratory of Metallogeny and Mineral Assessment, Institute of Mineral Resources, CAGS, Beijing 100037, China*
[2]*Institute for Mineralogy, Leibniz Universität Hannover, Callinstrasse 3, 30167 Hannover, Germany*
[3]*Mineral Resources, Technische Universität Clausthal, Adolph-Roemer-Strasse 2A, 38678 Clausthal-Zellerfeld, Germany*
[4]*Jinyuan Mining Industry Co., Ltd., Lingbao 472500, China*

Correspondence should be addressed to Wei Jian; weijian851@gmail.com

The recently developed technique of ultraviolet femtosecond laser ablation inductively coupled plasma mass spectrometry (UV-fs-LA-ICP-MS) combined with a freezing cell is expected to improve the analysis of CO$_2$-rich fluid inclusions by decreasing their internal pressure and avoiding the common problem of uncontrolled explosive fluid release on ablation. Here, we report the application of this technique through the case study of CO$_2$-rich fluid inclusions from the quartz vein-style Au-Mo deposit of Dahu in the Xiaoqinling region of central China. The concentrations of Li, B, Na, Al, K, Ca, Mn, Fe, Cu, Zn, Rb, Sr, Mo, Ag, Te, Cs, Ba, Au, Pb, and Bi were analyzed in 124 (not all for Al and Ca) fluid inclusions, which have low to moderate salinity and multiphase composition (liquid H$_2$O + liquid CO$_2$ ± vapor CO$_2$ ± solids). The Dahu fluids are dominated by Na and K. The concentrations of Mo are always below the detection limit from 0.005 to 2 ppm (excluding values obtained from fluid inclusions with accidentally trapped solids). The Dahu ore fluids differ from metamorphic fluids in compositions and most likely represent two separate pulses of spent fluids evolved from an unexposed and oxidized magmatic system. The UV-fs-LA-ICP-MS analysis of fluid inclusions in a frozen state improves the overpressure problem of CO$_2$-rich fluid inclusions during laser ablation. The transformation of gaseous and liquid CO$_2$ into the solid state leads to a significant decline in the internal pressure of the fluid inclusions, while femtosecond laser pulses generate a minimal heat input in the sample and thus maintain the frozen state during ablation. Transient signals of CO$_2$-rich fluid inclusions obtained in this study typically had one or multiple peaks lasting for more than 15 seconds, without an initial short signal spike as obtained by ns-LA-ICP-MS analysis of CO$_2$-rich fluid inclusions at room temperature.

1. Introduction

Laser ablation inductively coupled plasma mass spectrometry (LA-ICP-MS) is an efficient technique for multielement analysis of individual fluid inclusions (e.g., [1–4]). In the past two decades, this technique has been widely used to determine element concentrations of fluid inclusions, and a large dataset on fluid compositions has been produced for aqueous fluid inclusions which dominate the fluid inclusion populations in porphyry-type and many other hydrothermal ore deposits (e.g., [5–17]). In contrast, information on

element concentrations in low to moderate salinity (i.e., <15 wt.% NaCl equivalent) aqueo-carbonic fluid inclusions (i.e., CO$_2$ as one or two separate phases at room temperature), which are the dominant fluid inclusion type in the gold-bearing quartz veins in the Xiaoqinling region (e.g., [18–22]), as well as orogenic gold deposits (e.g., [23–25]) and some deep-seated intrusion-related gold deposits (e.g., [26–28]), is only fragmentary (e.g., [29–31]). One major challenge to analyzing solutes in CO$_2$-rich fluid inclusions by the LA-ICP-MS technique is the internal overpressure of such inclusions at room temperature. Because of their high internal pressure,

CO_2-rich fluid inclusions always show very short transient signals upon opening and more than 90% of the solute content is liberated during the first signal burst (e.g., [4]). Therefore, it is rather difficult to acquire utilizable transient signals for further data processing, resulting in low precision and accuracy.

Recently, Albrecht et al. [32] developed an ultraviolet femtosecond laser ablation inductively coupled plasma mass spectrometry (UV-fs-LA-ICP-MS) technique to analyze individual fluid inclusions in a frozen state. The combination of a 194 nm femtosecond laser and a heating-freezing cell as the laser cell results in much improved control during the opening of fluid inclusions, because the transformation of gaseous and liquid CO_2 into the solid state leads to a significant decline in the internal pressure of fluid inclusions. Therefore, this technique is expected to solve the overpressure problem of CO_2-rich fluid inclusion during laser ablation. Here, we report the application of this method by analyzing CO_2-rich fluid inclusions from the quartz vein-style Dahu Au-Mo deposit in the Xiaoqinling region of central China, with special emphasis on the fluid source of the Dahu Au-Mo deposit.

2. Geological Setting

The Xiaoqinling region, located at the southern margin of the North China craton, belongs to the Qinling–Dabie orogen, which delimits the boundary between the North China craton and the Yangtze craton (Figure 1; [39, 40]). The Qinling–Dabie orogen resulted from multistage collisional events between the North China craton and the Yangtze craton, the final collision of which took place in the Triassic (e.g., [40, 41]). During the Late Triassic, the Qinling–Dabie orogen evolved into a postcollisional extensional domain [40, 41].

The strata exposed in the Xiaoqinling region are dominated by Archean amphibolite-facies metamorphic rocks of the Taihua Group, which hosts most of the gold-bearing quartz veins. The Taihua Group consists of biotite plagiogneiss, amphibole plagiogneiss, amphibolite, quartzite, and marble [42]. These rocks probably formed in the Neoarchean and have been subjected to amphibolite-facies metamorphism in the Paleoproterozoic [43–45]. The Archean rocks were intruded by Paleoproterozoic pegmatite [45, 46], Paleoproterozoic and Early Cretaceous mafic dikes [47–49], and Proterozoic and Mesozoic granitic intrusions. Mesozoic granitic intrusions formed during the Late Triassic (228–215 Ma: [50, 51]) and the Early Cretaceous (146–131 Ma: [21, 51–56]) and are widely exposed in the Xiaoqinling region (Figure 1(a)).

The Xiaoqinling region has a proven Au reserve of more than 630 tonnes. Gold is mainly hosted in more than 1200 Au-bearing quartz veins [46] which also show a very pronounced Te signature (Te concentration in the gold ores is typically in the magnitude range of tens to hundreds of ppm: [21, 22, 57, 58]), and economic Mo concentrations were also found in Au-bearing quartz veins at the Dahu deposit and its adjacent area [22, 45, 59–63]. Gold-bearing quartz veins concentrate along the axes of several E–W-striking folds and are controlled by small to medium size (typically several kilometer long and several to dozens of meter wide) E–W-striking faults.

3. Deposit Geology and Timing of Mineralization

The quartz vein style Dahu Au-Mo deposit has proven reserves of 31 tonnes of Au (grade: 4.7 g/t Au) and 30,000 tonnes of Mo (grade: 0.13% Mo) [64]. This deposit is located on the northern side of the Wulicun anticline and hosted by biotite plagiogneiss, amphibole plagiogneiss, and amphibolite of the Archean Taihua Group (Figure 1). The Taihua Group was intruded by mafic dikes and granite porphyries. Bi et al. [49] reported a zircon LA-ICP-MS U-Pb age of 1816 ± 14 Ma for a mafic dike. The granite porphyry dikes that have not been dated yet are locally cut by mineralized quartz veins which are controlled by E–W-striking faults and dip to the NW at shallow to moderate angles (23–52°). Gold orebodies and Mo orebodies occur in different veins or in different parts of the same vein and locally overlap.

Mineralization of the Dahu deposit has been divided into four stages [22]: an initial quartz-K-feldspar stage (I) characterized by milky quartz and pink K-feldspar and minor coarse-grained (>5 mm) euhedral pyrite, anhydrite, celestine, covellite, rutile, and molybdenite (Figure 2), a pyrite-molybdenite stage (II) characterized by intergrowth of fine to very fine-grained (0.005–1 mm) pyrite and molybdenite, a sulfide-telluride–sulfosalt–gold stage (III) characterized by abundant galena and chalcopyrite and accessory celestine, native gold, tellurides, and Bi-sulfosalts (Figure 2), and a final barren carbonate-dominated stage (IV). Stages I and II are molybdenite deposition stages, while stage III is the gold deposition stage.

A molybdenite Re-Os isochron age of 206.4 ± 3.9 Ma [22] suggests that molybdenum mineralization occurred in the Late Triassic. The time of gold mineralization is not well constrained, but as shown above, petrographic observations indicate that gold precipitated later than molybdenite. Hydrothermal monazite intergrown with molybdenite yields SHRIMP U-Th-Pb ages ranging from 224.3 ± 3.3 to 101.1 ± 7.1 Ma, with a peak at 216 ± 5 Ma [60]. This led Li et al. [60] to propose that the 216 Ma age represents the time of monazite and molybdenite deposition while the younger and scattered ages are related to a 125 Ma hydrothermal event which partially disturbed the U-Th-Pb system in monazite and is also responsible for Au mineralization, although petrographic evidence is still required to link the monazite alteration process to Au mineralization.

4. Fluid Inclusion Characteristics

Petrographic, Raman spectroscopic, and microthermometric studies on fluid inclusions have been carried out by Jian et al. [22] and are briefly summarized below. H_2O-CO_2 fluid inclusions (liquid H_2O + liquid CO_2 ± vapor CO_2 ± solids) of low to moderate salinity (average 7.9 and 10.7 wt.% NaCl equivalent for stage I and III fluid inclusions, resp.) dominate
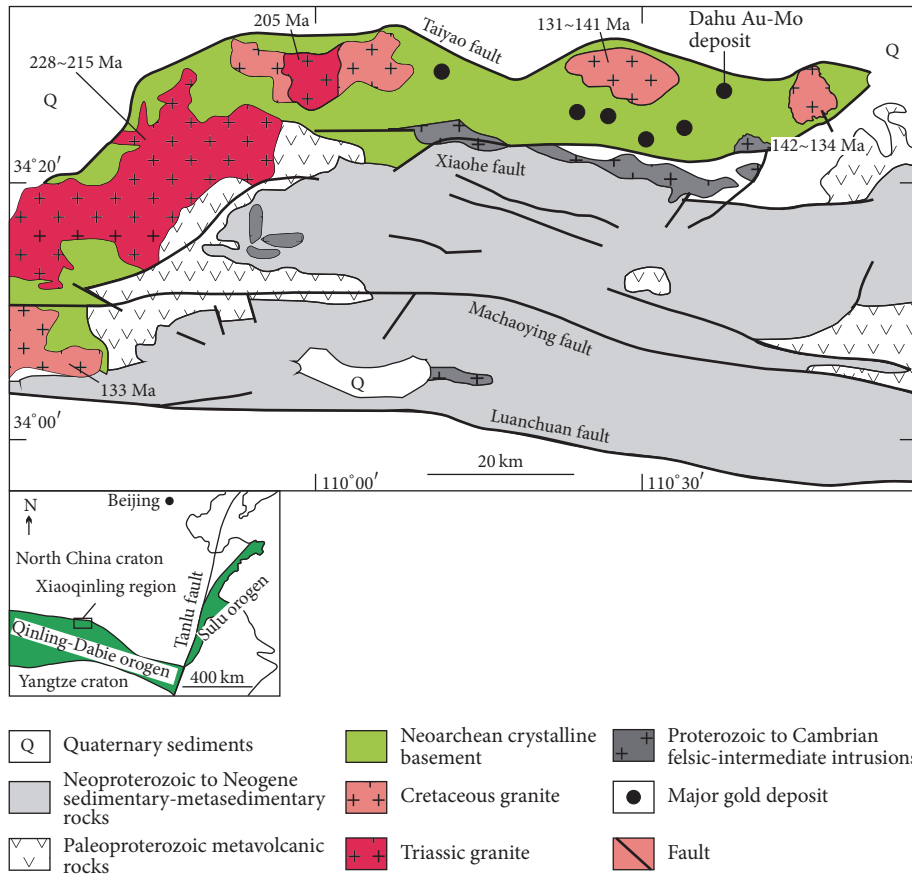
(a)
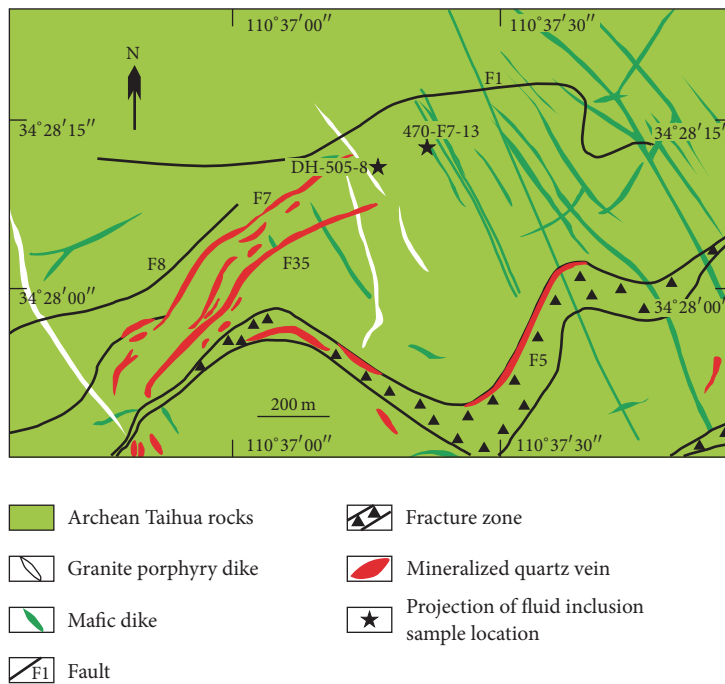
(b)

Figure 1: (a) Geologic map of the Xiaoqinling region and its position in China (after [22]). (b) Geologic map of the Dahu Au-Mo deposit (modified from [33]).
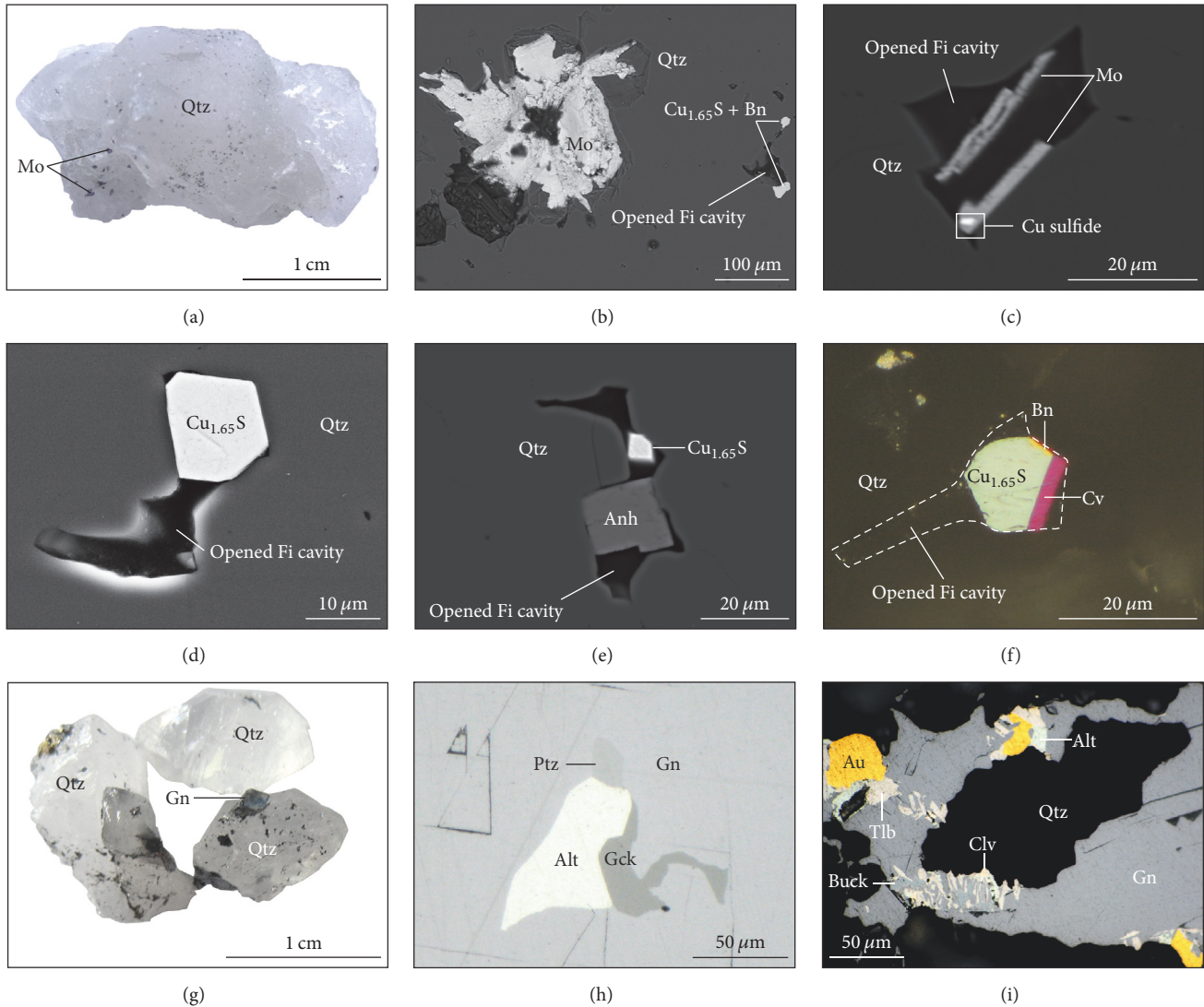
Figure 2: Vein mineralogy of Dahu stage I and stage III mineralization. (a) Stage I quartz crystals with abundant molybdenite mineral inclusions. Sample LS-540-3. (b) Backscattered electron (BSE) image showing molybdenite occurring as larger mineral inclusions in stage I quartz while $Cu_{1.65}S$ and bornite occur as smaller solids in opened fluid inclusions. Sample LS-540-3. (c)–(e) BSE images and (f) plane-polarized reflected light photomicrograph showing solids including molybdenite, $Cu_{1.65}S$, covellite, bornite, and anhydrite in opened fluid inclusions in stage I quartz. Sample LS-540-3. (g) Stage III quartz crystals in contact with galena. Sample 470-F7-13. (h) Plane-polarized reflected light photomicrograph showing aggregate of altaite, greenockite, and petzite in galena. Sample 470-F7-13. (i) Plane-polarized reflected light photomicrograph showing gold and tellurides in galena. Sample 400-10. Alt = altaite, Anh = anhydrite, Au = gold, Bn = bornite, Buck = buckhornite, Cv = covellite, Clv = calaverite, Fi = fluid inclusion, Gck = greenockite, Gn = galena, Mo = molybdenite, Ptz = petzite, Py = pyrite, Qtz = quartz, and Tlb = tellurobismuthite.

fluid inclusion populations in both stage I and stage III quartz (Figure 3) and are supposed to represent the ore fluids. Total homogenization temperatures of the H_2O-CO_2 fluid inclusions in stage I and stage III quartz range from 230 to 440°C and 198 to 320°C, respectively. Two-phase (liquid H_2O + vapor H_2O), low to moderate salinity H_2O fluid inclusions are less abundant than H_2O-CO_2 fluid inclusions. These fluid inclusions show a flat shape and all occur in planar groups. They postdate the H_2O-CO_2 fluid inclusions, with systematically lower total homogenization temperatures (143 to 204°C) and represent postmineralization fluids.

H_2O-CO_2 fluid inclusions in stage I quartz occasionally contain one or more solid phases (Figures 2 and 3). Electron microprobe analysis of the solid phases in opened fluid inclusions confirms the presence of $Cu_{1.65}S$, covellite, chalcopyrite, bornite, molybdenite, pyrite, colusite, anhydrite, and celestine [22].

All the solid phases observed in the H_2O-CO_2 fluid inclusions of the Dahu deposit are trapped crystals rather than daughter minerals based on the following reasons: (1) Solids occur only in a fraction of the H_2O-CO_2 fluid inclusions at the Dahu deposit, even for H_2O-CO_2 fluid inclusions
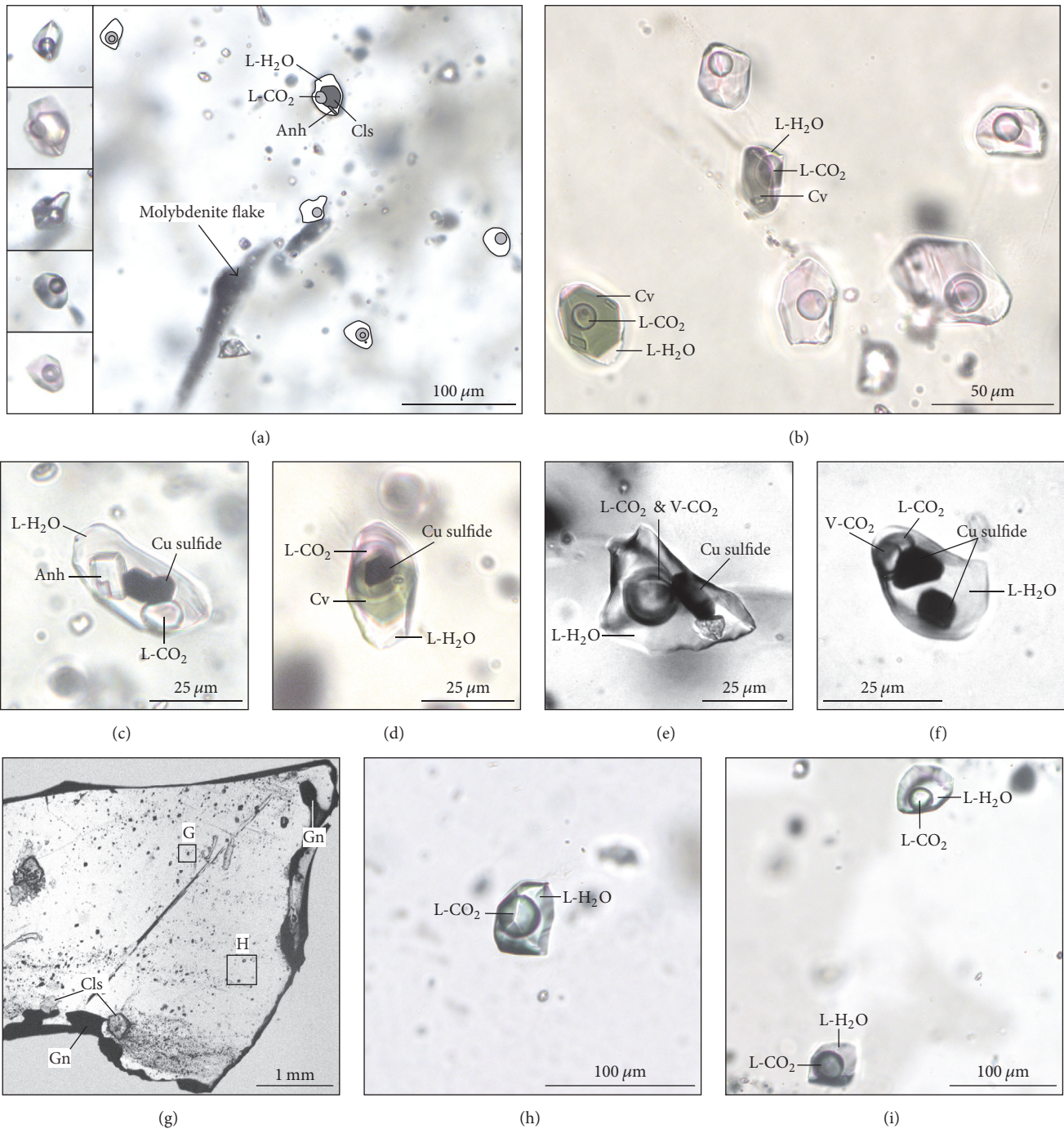
FIGURE 3: Photomicrographs of representative H_2O-CO_2 fluid inclusions used for UV-fs-LA-ICP-MS analysis. (a) Fluid inclusion assemblage adjacent to a molybdenite flake in stage I quartz. Photomicrographs of the outlined fluid inclusions are shown in the left. Sample LS-540-3. (b) Fluid inclusion assemblage with coexisting solid-bearing (covellite) and solid-free fluid inclusions in stage I quartz. Note covellite is translucent in transmitted light because it occurs as very thin flakes. This was created through focus stacking which combines 3 images taken at different focus distances in order to show all the fluid inclusions in focus. Sample LS-540-3. (c)–(f) Solid-bearing fluid inclusions in stage I quartz. Sample DH-505-8 and LS-540-3. (g) Distribution of fluid inclusions in a fragment of stage III quartz crystal. Areas indicated by letters are detailed in (h) and (i). Sample 470-F7-13. (h)-(i) Fluid inclusions in stage III quartz. Anh = anhydrite, Cv = covellite, Gn = galena, and Cls = celestine.

within the same fluid inclusion assemblage (Figures 3(a) and 3(b)), while daughter minerals should be ubiquitous in fluid inclusions [65]. (2) The numbers and species of solids, as well as the solid/fluid and solid/solid ratios (Figures 2 and 3), vary significantly among individual solid-bearing fluid inclusions at the Dahu deposit, while daughter mineral should occur in a regular ratio to other phases [65]. (3) Some solid-bearing fluid inclusions have very large solid/fluid ratio (Figures 2 and 3). If these solids are daughter minerals that precipitated from the fluids after trapping; the fluids must have dissolved several to tens of weight percent of sulfides and/or sulfates during the time of trapping. This is highly unrealistic. (4) Minerals present as solids in fluid inclusions have also been observed as mineral inclusions in stage I quartz or as anhedral aggregates in stage I quartz microfractures. According to Roedder [65], these solid-bearing fluid inclusions observed at the Dahu deposit can also be called composite inclusions. Accordingly, these inclusions do not represent the true composition of the fluid during the time of trapping because of the presence of accidentally trapped crystals.

5. Sample Material and Preparation

H_2O-CO_2 fluid inclusions in five double polished thick sections were firstly examined under the microscope and then were used to carry out microthermometric measurements and UV-fs-LA-ICP-MS analysis. The samples are located in Figure 1. Sections DH-505-8, LS-540-3B, and LS-540-3C were made from stage I quartz crystals collected from the Mo orebody. The quartz crystals contain abundant molybdenite mineral inclusions, which typically range from 100 to 200 μm in length (Figures 2(a), 2(b), and 3(a)). Sections 470-F7-13A and 470-F7-13D were made from stage III quartz crystals which contain abundant celestine mineral inclusions and are enclosed by galena. The two sections were prepared from an Au ore sample consisting of quartz, galena, and minor altaite, hessite, and petzite, a common gold-bearing mineral.

6. Analytical Techniques

Fluid inclusion microthermometric measurements were carried out at Technische Universität Clausthal, Germany, using a Linkam THMS 600 heating-freezing stage. CO_2-H_2O clathrate melting temperatures obtained by microthermometry were used to calculate the NaCl equivalent values [66], which were subsequently used as an internal standard to transform the element ratios measured by UV-fs-LA-ICP-MS into absolute concentrations using the SILLS data reduction software [67]. The calculation procedure includes a salt correction which balances the influence of other major cations such as K in the fluid for the NaCl equivalent values.

Ultraviolet femtosecond laser ablation inductively coupled plasma mass spectrometry (UV-fs-LA-ICP-MS) was carried out at Leibniz Universität Hannover, Germany. Details on the instrumentation and analytical procedure can be found in Albrecht et al. [32] and are briefly summarized below. An Element XR™ fast scanning sector field inductively coupled plasma mass spectrometer was used in combination with an in-house built laser ablation system which is based

on a Spectra-Physics™ Solstice femtosecond laser. The laser system operates in the deep UV at 194 nm and produces pulse energy of 70–90 μJ in the fourth harmonic. This ultra short pulsed laser generates a soft ablation with high control and minimizes elemental fractionation at the sample site [68–71].

Quartz chips and standard reference materials were placed in a modified heating-freezing cell, which enables laser ablation at low temperatures. Quartz chips were first quickly cooled to a temperature of $-110°C$ to ensure that fluid inclusions became completely frozen. Afterwards, laser ablation was performed at -65 to $-60°C$, that is, below the CO_2 triple point of $-56.6°C$. The ablation of the standard reference material NIST 610 was carried out with a repetition rate of 10 Hz. The sample surface was carefully precleaned by a few shots with a repetition rate of 2 Hz. Silicon was used as the matrix-only tracer for the separation of the fluid inclusion signal from the quartz signal.

Depending on the size of fluid inclusions, two different approaches were used for ablation. For both approaches, the beam size was held constant during the ablation process. For fluid inclusions smaller than 30 μm in diameter, a fixed spot ablation technique (i.e., the laser beam was fixed in position during ablation) was used. The selected beam size was bigger than the analyzed fluid inclusion to guarantee that the whole fluid inclusion material was mobilized and subsequently transported to the ICP-MS. Depending on the depth of fluid inclusions beneath sample surface, a repetition rate of 2 to 10 Hz was used. The concentrations of 18 elements ([7]Li, [11]B, [23]Na, [39]K, [55]Mn, [57]Fe, [65]Cu, [66]Zn, [85]Rb, [88]Sr, [95]Mo, [107]Ag, [125]Te, [133]Cs, [137]Ba, [197]Au, [208]Pb, and [209]Bi) were measured in each individual fluid inclusion. The sample time for Au was 10 ms for samples 470-F7-13A and 470-F7-13D, and 3 ms for sample DH-505-8. For all other elements, the sample time was set to 3 ms per line, resulting in a total sweep time of 504 ms for sample DH-505-8 and 532 ms for samples 470-F7-13A and 470-F7-13D.

For fluid inclusions bigger than 30 μm in diameter, a fast moving spiral ablation technique was used. This technique is based on the open source software LinuxCNC, allowing the user to create laser patterns adjustable to the sample. This approach allows the analysis of larger fluid inclusions by rapidly moving the laser beam in a repeated spiral pattern. The overall ablated area is bigger than the analyzed fluid inclusion to guarantee that all fluid inclusion material gets mobilized and subsequently transported to the ICP-MS instrument. Depending on the depth of fluid inclusions beneath sample surface, a repetition rate of 100 to 500 Hz was used. Due to the higher repetition rate and the larger sample volumes, the calculated detection limits are expected to decrease significantly and the observed signal intensities and durations are expected to increase compared to the fixed spot ablation technique. Thus, it is possible to increase the sample time for the 20 measured elements ([7]Li, [11]B, [23]Na, [27]Al, [39]K, [44]Ca, [55]Mn, [57]Fe, [65]Cu, [66]Zn, [85]Rb, [88]Sr, [95]Mo, [107]Ag, [125]Te, [133]Cs, [137]Ba, [197]Au, [208]Pb, and [209]Bi) to 10 ms per line with 4 lines per peak, resulting in a total sweep time of 707 ms.

By using the two different approaches, 124 H_2O-CO_2 fluid inclusions, covering a size range between 13 and 50 μm and a depth range between 5 and 120 μm, have been successfully analyzed. UV-fs-LA-ICP-MS data for fluid inclusions are reported below and shown in Tables 1 and A1.

7. Results

7.1. Stage I Fluid Inclusions. For solid-free fluid inclusions in stage I quartz, B, Na, K, Rb, and Cs are always present in detectable concentrations, while Ca, Fe, Mo, Ag, Te, and Bi are always below detection limits (Table 2). Lithium and Sr were detected in most of the measured fluid inclusions, while Al, Mn, Cu, Zn, Ba, Au, and Pb were detected in a small number of the fluid inclusions. As suggested by Pettke et al. [4, 72], the fluid composition is best characterized as the average plus external uncertainty obtained from a series of analyzed fluid inclusions belonging to a homogeneously entrapped fluid inclusion assemblage. Therefore, the UV-fs-LA-ICP-MS data for solid-free fluid inclusions in stage I quartz are reported as average element concentrations of fluid inclusion assemblages (FIA) below and summarized in Table 1. Sodium is always the dominant cation (14842–43914 ppm), followed by K (3286–14165 ppm) and B (71–502 ppm). The concentrations of alkali elements including Li (<0.8 to 531 ppm), Rb (21–83 ppm), and Cs (7–46 ppm) and earth alkaline elements including Sr (4–91 ppm) and Ba (<0.006 to 44 ppm) are typically in the range of several to tens of ppm. The concentrations of base metals including Cu, Zn, and Pb are mostly below their analytical detection limits at the ppm level. Exceptional values reach up to 56 ppm Cu, 173 ppm Zn, and 31 ppm Pb. The concentrations of Al and Mn range from <0.07 to 243 ppm and <0.3 to 158 ppm, respectively. Gold was only detected in one individual fluid inclusion (Au: 1 ppm) but without showing a distinct peak in the time-resolved ICP-MS signal.

For solid-bearing fluid inclusions (i.e., composite inclusions or fluid inclusions with accidentally trapped solids), the data are reported as the element concentrations of individual fluid inclusions instead of FIAs and are shown in Table A1. In general, these inclusions often contain elevated but highly variable concentrations of Cu, Mo, Ag, Ca, and Sr due to the presence of accidentally trapped crystals of $Cu_{1.65}S$, covellite, chalcopyrite, molybdenite, anhydrite, and celestine. Since the composition of these inclusions do not represent the true composition of the fluids and the relatively low Na/metal ratios of these inclusions can result in large errors for the elemental concentration data (calculated based on NaCl equivalent values), the elemental concentration data for these inclusions are for reference only and will not be further discussed.

7.2. Stage III Fluid Inclusions. All the UV-fs-LA-ICP-MS data for stage III fluid inclusions are from solid-free fluid inclusions, because solids are rarely present in these fluid inclusions.

In all measured fluid inclusions of stage III quartz, B, Na, K, Rb, Sr, Cs, and Pb are present in detectable concentrations, while Ca, Mo, Te, Au, and Bi are always below their detection

limits (Table 1). Lithium, Zn, and Ba were detected in most of the measured fluid inclusions, while Al, Mn, Fe, Cu, and Ag were detected in a small part of the measured fluid inclusions.

The UV-fs-LA-ICP-MS data are briefly reported as average element concentrations of FIA below and detailed in Table 1. Like solid-free fluid inclusions in stage I quartz, fluid inclusions in stage III quartz are dominated by Na (24203–34761 ppm) and K (9869–16592) with subordinate amount of B (130–527 ppm). The concentrations of alkali elements including Li (31–57 ppm), Rb (28–64 ppm), and Cs (5–13 ppm) and earth alkaline elements including Sr (20–76 ppm) and Ba (2–10 ppm) are all in the range of several to tens of ppm. The concentrations of Zn and Pb range from 13 to 58 ppm and 19 to 120 ppm, respectively. The concentrations of Cu are mostly below the analytical detection limits at the ppm level. Exceptional values reach up to 179 ppm Cu.

8. Discussion

8.1. Strengths of the UV-fs-LA-ICP-MS Technique. The greatest advantage of UV-fs-LA-ICP-MS analysis of CO_2-rich fluid inclusions in a frozen state is that this technique can improve the overpressure problem of CO_2-rich fluid inclusions during laser ablation. CO_2-rich fluid inclusions can have large internal pressure at room temperature. Owing to the pressure release upon fluid inclusion opening, nanosecond LA-ICP-MS analysis of CO_2-rich fluid inclusions at room temperature tends to show an extremely fast transient signal spike (e.g., <3 seconds: [4, 73]) at the beginning of a fluid inclusion signal, followed by a signal hump produced by the remaining fluid inclusion content. Because more than 90% of the solute content is liberated during the first signal burst, it is difficult to representatively record the initial fast transient signal peak that dominates the bulk solute signal. Through UV-fs-LA-ICP-MS analysis of CO_2-rich fluid inclusions in a frozen state, the impact from fluid inclusion overpressure can be reduced. This is because phase transformation of vapor and liquid CO_2 to solid CO_2 at low temperature can significantly decrease the internal pressure of fluid inclusions, while femtosecond laser pulses can minimize the heat transfer from the laser spot into the sample, thus keeping fluid inclusions in a frozen state during ablation. Transient signals of CO_2-rich fluid inclusions obtained in this study typically show one or multiple peaks lasting more than 15 seconds (e.g., Figure 4). This time span is much longer than the signal spike (e.g., <3 seconds) obtained by LA-ICP-MS analysis of CO_2-rich fluid inclusions at room temperature, thus enabling recording of more sampling cycles.

Other advantages of UV-fs-LA-ICP-MS analysis of CO_2-rich fluid inclusions in a frozen state include its ability to analyze very shallow fluid inclusions. Such very shallow fluid inclusions usually explode upon opening at room temperature. The ultra short pulsed laser system with its small ablation rate (10 nm/puls) generates a smooth ablation on quartz, without creating cracks or knocking-out bigger fragments. For example, fluid inclusions as shallow as 5 μm have been successfully analyzed in this study (e.g., Figure 4). Furthermore, because the explosion of fluid inclusions is excluded when they are frozen, there is no need for a stepwise

TABLE 1: Element concentrations (ppm) in solid-free fluid inclusion assemblages (FIA) from Dahu stage I and stage III quartz.

(a)

FIA	N	Li	SD (n)	B	SD (n)	Na	SD (n)	Al	SD (n)	K	SD (n)	Ca	SD (n)	Mn	SD (n)
						Stage I									
						Sample: DH-505-8									
A1	4	20	3 (2)	264	71 (4)	21694	4257 (4)	NM	NM	8417	1716 (4)	NM	NM	30	- (1)
A2	2	88	19 (2)	424	79 (2)	26733	747 (2)	NM	NM	7155	291 (2)	NM	NM	81	- (1)
A3	3	235	- (1)	502	28 (3)	27928	2604 (3)	NM	NM	10086	1407 (3)	NM	NM	158	- (1)
A4	2	31	10 (2)	177	2 (2)	17649	4808 (2)	NM	NM	4406	197 (2)	NM	NM	18	- (1)
A5	6	33	16 (4)	172	52 (6)	17875	2001 (6)	<2	- (0)	6398	643 (6)	<167	- (0)	10	3 (3)
A6	4	25	11 (3)	156	13 (4)	15746	1586 (4)	NM	NM	5887	567 (4)	NM	NM	<6	- (0)
A7	6	30	15 (6)	217	38 (6)	21879	2657 (6)	NM	NM	6491	1313 (6)	NM	NM	14	8 (4)
A9	7	27	9 (4)	126	62 (7)	19029	2031 (7)	112	- (1)	5439	616 (7)	<20	- (0)	22	7 (4)
A10	4	19	2 (2)	149	16 (4)	14842	1980 (4)	243	- (1)	6839	954 (4)	<47	- (0)	6	- (1)
A11	1	72	- (1)	251	- (1)	21121	- (1)	NM	NM	3286	- (1)	NM	NM	<3	- (0)
A12	1	<10	- (0)	169	- (1)	22913	- (1)	NM	NM	4787	- (1)	NM	NM	24	- (1)
A13	1	<20	- (0)	357	- (1)	19377	- (1)	NM	NM	5047	- (1)	NM	NM	<12	- (0)
A14	1	23	- (1)	164	- (1)	18603	- (1)	NM	NM	5227	- (1)	NM	NM	9	- (1)
A15	1	74	- (1)	145	- (1)	17100	- (1)	NM	NM	5307	- (1)	NM	NM	<8	- (0)
						Stage I									
						Sample: LS-540-3B									
B1	4	531	273 (4)	71	8 (4)	18078	993 (4)	32	15	11304	519 (4)	<11	- (0)	12	2 (2)
B2	1	<0.8	- (0)	123	- (1)	20609	- (1)	<0.07	- (0)	10980	- (1)	<5	- (0)	<0.3	- (0)
						Stage I									
						Sample: LS-540-3C									
C1	4	84	6 (2)	167	28 (4)	43914	10113 (4)	<0.8	- (0)	14165	4390 (4)	<59	- (0)	25	- (1)
						Stage III									
						Sample: 470-F7-13D									
D1	6	47	4 (6)	370	45 (6)	34485	1309 (6)	NM	NM	14635	1543 (6)	NM	NM	25	12 (2)
D2	7	44	7 (7)	337	36 (7)	32528	3648 (7)	NM	NM	12387	1705 (7)	NM	NM	28	1 (3)
D3	13	45	12 (12)	283	57 (13)	34755	1408 (13)	128	112 (5)	15105	1089 (13)	<23	- (0)	11	12 (5)
D4	8	47	6 (7)	254	53 (8)	33922	3565 (8)	145	68 (2)	14449	2761 (8)	<23	- (0)	3.2	1 (3)
D5	2	49	10 (2)	321	9 (2)	34761	1250 (2)	NM	NM	12905	570 (2)	NM	NM	23	- (1)
D6	1	57	- (1)	339	- (1)	34265	- (1)	NM	NM	16592	- (1)	NM	NM	<4	- (0)
						Stage III									
						Sample: 470-F7-13A									
E1	4	31	10 (4)	130	77 (4)	31373	3173 (4)	NM	NM	9869	4386 (4)	NM	NM	44	- (1)
E2	7	44	7 (7)	527	238 (7)	29782	2370 (7)	NM	NM	12155	1476 (7)	NM	NM	19	- (1)
E3	1	38	- (1)	149	- (1)	24203	- (1)	NM	NM	10355	- (1)	NM	NM	24	- (1)

(b)

FIA	N	Fe	SD (n)	Cu	SD (n)	Zn	SD (n)	Rb	SD (n)	Sr	SD (n)	Mo	SD (n)	Ag	SD (n)
						Stage I									
						Sample: DH-505-8									
A1	4	<88	- (0)	56	- (1)	<7	- (0)	83	20 (4)	16	5 (4)	<0.8	- (0)	<0.6	- (0)
A2	2	<95	- (0)	<3	- (0)	63	9 (2)	53	4 (2)	37	17 (2)	<0.9	- (0)	<0.8	- (0)
A3	3	<114	- (0)	<4	- (0)	173	- (1)	69	16 (3)	91	6 (3)	<1	- (0)	<1	- (0)
A4	2	<53	- (0)	<2	- (0)	<4	- (0)	41	2 (2)	7	1 (2)	<0.4	- (0)	<0.5	- (0)
A5	6	<40	- (0)	7	- (1)	<3	- (0)	61	11 (6)	15	12 (6)	<0.3	- (0)	<0.3	- (0)
A6	4	<70	- (0)	5	- (1)	<5	- (0)	42	14 (4)	8	4 (4)	<0.7	- (0)	<0.6	- (0)
A7	6	<53	- (0)	<2	- (0)	15	- (1)	54	8 (6)	10	3 (6)	<0.5	- (0)	<0.5	- (0)
A9	7	<32	- (0)	<1	- (0)	8	- (1)	37	5 (7)	11	5 (7)	<0.3	- (0)	<0.3	- (0)
A10	4	<55	- (0)	<2	- (0)	<4	- (0)	31	2 (4)	8	3 (4)	<0.4	- (0)	<0.5	- (0)
A11	1	<33	- (0)	<1	- (0)	<2	- (0)	21	- (1)	4	- (1)	<0.3	- (0)	<0.3	- (0)
A12	1	<64	- (0)	<2	- (0)	<4	- (0)	34	- (1)	9	- (1)	<0.5	- (0)	<0.6	- (0)

(b) Continued.

	N		SD (n)		SD (n)		SD (n)		SD (n)		SD (n)		SD (n)		SD (n)
A13	1	<139	- (0)	<5	- (0)	<10	- (0)	36	- (1)	21	- (1)	<1	- (0)	<1	- (0)
A14	1	<45	- (0)	<2	- (0)	<3	- (0)	46	- (1)	11	- (1)	<0.4	- (0)	<0.4	- (0)
A15	1	<95	- (0)	<4	- (0)	<7	- (0)	41	- (1)	13	- (1)	<0.9	- (0)	<0.8	- (0)
Stage I															
Sample: LS-540-3B															
B1	4	<5	- (0)	<0.6	- (0)	<0.2	- (0)	35	2 (4)	5	1 (4)	<0.03	- (0)	<0.04	- (0)
B2	1	<2	- (0)	<0.2	- (0)	<0.07	- (0)	70	- (1)	15	- (1)	<0.01	- (0)	<0.02	- (0)
Stage I															
Sample: LS-540-3C															
C1	4	<8	- (0)	13	- (1)	<0.3	- (0)	71	16 (4)	14	5 (3)	<0.05	- (0)	<0.07	- (0)
Stage III															
Sample: 470-F7-13D															
D1	6	<54	- (0)	<1	- (0)	58	28 (6)	52	3 (6)	73	18 (6)	<0.3	- (0)	<0.4	- (0)
D2	7	104	- (1)	6	- (1)	39	12 (7)	58	11 (7)	76	14 (7)	<0.3	- (0)	<0.3	- (0)
D3	13	51	- (1)	<0.6	- (0)	55	21 (13)	48	6 (13)	62	39 (13)	<0.1	- (0)	0.4	0.3 (4)
D4	8	<28	- (0)	<0.7	- (0)	34	15 (7)	50	10 (8)	40	11 (8)	<0.1	- (0)	0.4	- (1)
D5	2	<64	- (0)	<2	- (0)	52	7 (2)	64	5 (2)	72	0.1 (2)	<0.4	- (0)	<0.5	- (0)
D6	1	<32	- (0)	<0.8	- (0)	38	- (1)	50	- (1)	60	- (1)	<0.1	- (0)	<0.2	- (0)
Stage III															
Sample: 470-F7-13A															
E1	4	<63	- (0)	179	- (1)	13	3 (4)	28	6 (4)	33	16 (4)	<0.4	- (0)	<0.5	- (0)
E2	7	<98	- (0)	<3	- (0)	52	34 (7)	50	7 (7)	38	25 (7)	<0.6	- (0)	<0.8	- (0)
E3	1	<60	- (0)	<2	- (1)	21	- (1)	36	- (1)	20	- (1)	<0.3	- (0)	<0.4	- (0)

(c)

FIA	N	Te	SD (n)	Cs	SD (n)	Ba	SD (n)	Au	SD (n)	Pb	SD (n)	Bi	SD (n)
Stage I													
Sample: DH-505-8													
A1	4	<5	- (0)	26	8 (4)	<1	- (0)	<1	- (0)	5	5 (3)	<0.2	- (0)
A2	2	<5	- (0)	43	2 (2)	9	5 (2)	<1	- (0)	14	15 (2)	<0.1	- (0)
A3	3	<6	- (0)	46	13 (3)	44	- (1)	<1	- (0)	31	16 (2)	<0.2	- (0)
A4	2	<3	- (0)	12	0.1 (2)	<0.7	- (0)	<0.6	- (0)	0.7	- (1)	<0.1	- (0)
A5	6	<2	- (0)	16	4 (6)	1	- (1)	<0.5	- (0)	2	1 (5)	<0.07	- (0)
A6	4	<4	- (0)	11	3 (4)	<0.9	- (0)	<0.8	- (0)	1	1 (2)	<0.1	- (0)
A7	6	<3	- (0)	15	2 (6)	1	1 (3)	<0.6	- (0)	2	1 (5)	<0.1	- (0)
A9	7	<2	- (0)	13	3 (7)	<0.4	- (0)	1	- (1)	2	2 (4)	<0.06	- (0)
A10	4	<3	- (0)	11	1 (4)	3	- (1)	<0.7	- (0)	0.4	0.03 (2)	<0.08	- (0)
A11	1	<2	- (0)	9	- (1)	<0.5	- (0)	<0.4	- (0)	<0.1	- (1)	<0.1	- (0)
A12	1	<3	- (0)	13	- (1)	3	- (1)	<0.8	- (0)	1	- (0)	<0.1	- (0)
A13	1	<7	- (0)	27	- (1)	<2	- (0)	<2	- (0)	<0.3	- (1)	<0.2	- (0)
A14	1	<3	- (0)	14	- (1)	0.9	- (1)	<0.5	- (0)	1	- (0)	<0.1	- (0)
A15	1	<5	- (0)	11	- (1)	<1	- (0)	<1	- (0)	<0.2	- (1)	<0.1	- (0)
Stage I													
Sample: LS-540-3B													
B1	4	<0.2	- (0)	7	1 (4)	<0.03	- (0)	<0.05	- (0)	<0.02	- (0)	<0.007	- (0)
B2	1	<0.06	- (0)	14	- (1)	<0.006	- (0)	<0.02	- (0)	<0.005	- (0)	<0.003	- (0)
Stage I													
Sample: LS-540-3C													
C1	4	<0.2	- (0)	13	3 (4)	34	- (1)	<0.09	- (0)	8	- (1)	<0.006	- (0)
Stage III													
Sample: 470-F7-13D													
D1	6	<2.3	- (0)	6	1 (6)	8	6 (6)	<0.3	- (0)	90	28 (6)	<0.1	- (0)
D2	7	<2.0	- (0)	8	3 (7)	10	7 (7)	<0.3	- (0)	120	83 (7)	<0.1	- (0)
D3	13	<1	- (0)	5	1 (13)	10	12 (10)	<0.2	- (0)	100	21 (13)	<0.04	- (0)
D4	8	<1	- (0)	6	1 (8)	4	1 (5)	<0.2	- (0)	68	43 (8)	<0.04	- (0)

(c) Continued.

D5	2	<2.8	- (0)	7	2 (2)	6	4 (2)	<0.4	- (0)	100	37 (2)	<0.1	- (0)
D6	1	<1.4	- (0)	5	- (1)	7	- (1)	<0.2	- (0)	88	- (1)	<0.1	- (0)
Stage III												
Sample: 470-F7-13A												
E1	4	<3	- (0)	5	1 (4)	2	1 (4)	<0.4	- (0)	22	10 (4)	<0.1	- (0)
E2	7	<4	- (0)	13	4 (7)	5	3 (6)	<0.5	- (0)	39	16 (7)	<0.1	- (0)
E3	1	<3	- (0)	8	- (1)	3	- (1)	<0.3	- (0)	19	- (1)	<0.1	- (0)

N = number of analyzed inclusions, n = number of significant concentrations, NM = not measured, and SD = standard deviation.
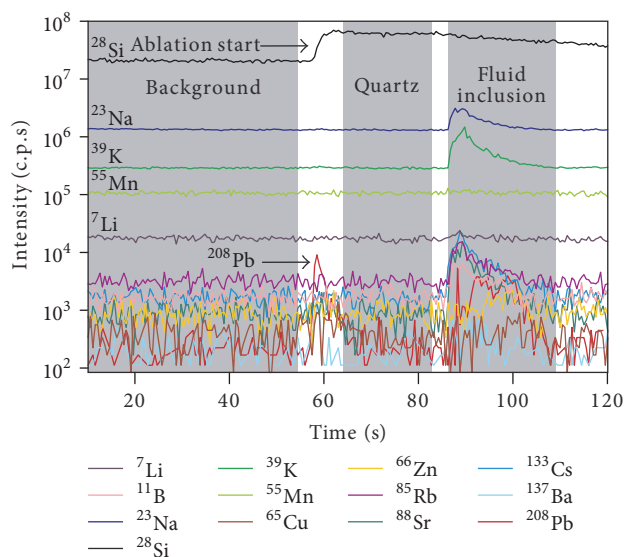
FIGURE 4: Time-resolved ICP-MS signal of a H_2O-CO_2 fluid inclusions in stage I quartz. This fluid inclusion is $20 \times 12\,\mu m$ in size and $5\,\mu m$ below sample surface. Note a distinct Pb peak caused by surface contamination (sample polishing material contains Pb) at the beginning of ablation, but it is easy to separate this Pb peak from the Pb peak generated by the fluid inclusion. "Background," "quartz," and "fluid inclusion" refer to the respective signal intervals used for quantification.

opening of fluid inclusions (e.g., [1]), making it easier to separate the surface contamination signal from the fluid inclusion signal (e.g., Figure 4).

8.2. *Interpretation of the Concentrations of Mo and Au.* All analyzed solid-free H_2O-CO_2 fluid inclusions in stage I (the molybdenite precipitation stage) quartz contain less than detectable concentrations of Mo (detection limit from 0.005 to 2 ppm). Such low Mo concentration (<2 ppm) are not only much lower than Mo concentrations reported in the fluids of porphyry Mo deposits (200–400 ppm) or porphyry Cu-(Mo-Au) deposits (10–600 ppm), but also lower than Mo concentrations reported in the fluids of barren granite (5–90 ppm; [38] and references therein).

The stage I quartz crystals used for UV-fs-LA-ICP-MS analysis carry abundant molybdenite mineral inclusions which show close spatial associations with the analyzed H_2O-CO_2 fluid inclusions (Figures 2(a), 2(b), and 3(a)),

and molybdenite was also observed as solid in opened fluid inclusions (Figure 2(c)). One possible explanation for the low concentrations of Mo and other elements of the ore mineral assemblage (e.g., Ca, Fe, Cu, Sr, and Mo) is that all analyzed H_2O-CO_2 fluid inclusions in stage I quartz represent the spent ore fluids that became trapped after the precipitation of the major sulfides (e.g., molybdenite) and sulfates (e.g., anhydrite) had already taken place. Therefore, most of the ore elements had already been lost from the fluids before their trapping in fluid inclusions. Consequently, ore components (e.g., Ca, Fe, Cu, Sr, and Mo) only show elevated concentrations in H_2O-CO_2 fluid inclusions with accidentally trapped solids, while solid-free fluid inclusions show very low metal contents.

Gold was detected in one individual fluid inclusion in stage I quartz with a questionable concentration value of 1 ppm (i.e., without visible Au peak in the time-resolved ICP-MS signal), while all the analyzed fluid inclusions in stage III quartz, which formed during the Au precipitation stage and which are enclosed by galena (the major Au carrier, Figures 2(g)–2(i)), contain less than detectable concentrations of Au (detection limit from 0.008 to 3 ppm). Nevertheless, fluids with only 3 to 15 ppb of Au are considered to be capable of forming Au deposit (e.g., [65, 74, 75]), although much higher Au concentrations in fluids have also been reported in Au deposits (e.g., up to 10 ppm of Au from the Grasberg porphyry Cu-Au deposits [8]).

8.3. *Two Separate Pulses of Fluids.* Dahu stage I (molybdenite deposition stage) fluid inclusions clearly differ from stage III (gold deposition stage) fluid inclusions by the presence of abundant solid phases. Excluding the fluid composition data obtained from solid-bearing fluid inclusions, stage I fluids still differ from stage III fluids by containing two times more Cs, ten times less Pb, two times less Sr, and lower concentrations of Na and K.

The systematically higher concentrations of Pb, Sr, Na, and K in stage III fluids compared to stage I fluids suggest that stage III fluids did not evolve from stage I fluids through metal precipitation or mixing with dilute meteoric groundwater, while the lower concentrations of Cs in stage III fluids imply that stage III fluids cannot represent the higher salinity brine formed by stage I fluids through phase separation, because Cs is partitioned preferentially into the brine phase instead of the vapor phase during fluid immiscibility (e.g., [38]). Therefore, we propose that stage I and stage III fluids, and by analogy the

TABLE 2: Detection limits (ppm) for each element measured by LA-ICP-MS.

	Li⁷	B¹¹	Na²³	Al²⁷	Si²⁸	K³⁹	Ca⁴⁴	Mn⁵⁵	Fe⁵⁷	Cu⁶⁵	Zn⁶⁶	Rb⁸⁵	Sr⁸⁸	Mo⁹⁵	Ag¹⁰⁷	Te¹²⁵	Cs¹³³	Ba¹³⁷	Au¹⁹⁷	Pb²⁰⁸	Bi²⁰⁹
Fixed spot ablation technique																					
Min	2	2	14	NM	130	4	NM	3	31	0.8	1	0.3	0.1	0.1	0.2	1	0.1	0.3	0.2	0.1	0.03
Max	32	30	158	NM	1570	33	NM	20	215	7	15	3	1	2	2	11	1	3	3	0.4	0.3
Spiral ablation technique																					
Min	0.3	0.03	0.1	0.03	1.2	0.1	2	0.1	0.7	0.1	0.02	0.003	0.003	0.005	0.006	0.02	0.001	0.003	0.008	0.002	0.001
Max	15	7	27	7	1046	15	526	7	81	2	3	2	0.3	0.4	0.6	2	0.3	0.5	0.8	0.1	0.1

NM = not measured.

fluids responsible for Mo and Au mineralization, represent two separate pulses of fluids.

8.4. Comparisons with Magmatic and Metamorphic Fluids.

Despite the differences in element concentrations between the Dahu stage I and III fluids, both stages of fluids are characterized by high K/Na weight ratios (0.16–0.63 and 0.31–0.48, respectively), which are much higher than those of metamorphic fluids (0.01 to 0.04: [35, 36]) but similar to those of the ore fluids from magmatic-hydrothermal deposits (e.g., fluids in porphyry and intrusion-related deposits: [9–12, 15, 17, 37, 38]). Rubidium concentrations of the Dahu ore fluids (21–83 and 28–71 ppm for stage I and stage III fluids, resp.) are also systematically higher than those of metamorphic fluids (0.6–9 ppm: [35, 36]).

In the K/Na versus Na + K, Rb/Na versus Na + K, and K versus Rb diagrams (Figure 5), the Dahu ore fluids clearly differ from metamorphic fluids but show close affinities to the ore fluids of magmatic-hydrothermal deposits. An unified explanation for the notably high K/Na ratio in magmatic fluids is difficult, because factors including fluid/rock ratio [65], the presence or absence of the albite-K-feldspar buffer [76], the temperature of water-rock interaction [77], and the contents of CO_2 and sulfates in fluids [78, 79] can all influence the K/Na ratio in fluids. Perhaps, magmatic fractionation processes and the higher temperature (i.e., compared to that of meteoric waters, basinal fluids, and most metamorphic fluids, [80]) of magmatic fluids are the two important factors which lead to the relative high K/Na ratio in magmatic fluids. During magmatic fractionation, the concentrations of K and Na generally increase, but K increases relatively more than Na in the residual melt, resulting in a steady increase of the K/Na ratio in the residual melt, and consequently an increase of the K/Na ratio in the fluid in equilibrium with the residual melt [81]. Temperature, on the other hand, influences the fluid K/Na ratio through the albite-K-feldspar buffer. The exchange of K and Na between fluid and albite-K-feldspar (the two minerals commonly coexist in a wide range of hydrothermally altered rocks) is temperature dependent; a process results in an increasing K/Na ratio of the fluid with increasing temperature of equilibration with the coexisting alkali feldspars [76, 77].

Apart from the metal concentrations, the precipitation of sulfates during both stage I and III mineralization and the absence of reduced gases in both stage I and III fluids inclusions (i.e., reduced gases such as CH_4 and N_2 were not detected in fluid inclusions by Raman spectroscopic analysis, [22, 61]) indicates a high oxidation state of the Dahu ore fluids, a characteristic which resembles the fluids from porphyry system and oxidized intrusion-related deposits (e.g., [82–85]) but differs from metamorphic fluids, which are normally reduced because of the common presence of organic materials and graphite in crustal rocks (e.g., [86]). Oxidized metamorphic fluids might be derived locally from sulfate-bearing evaporites, which, however, have not been reported in the Archean Taihua rocks. But the Taihua rocks, the crystalline basement rocks of the Xiaoqinling region and the host rocks of the Dahu deposit are locally rich in graphite [42].

The spent ore fluid hypothesis, as discussed before, suggests that the original fluids responsible for stage I and possibly stage III mineralization must have contained much higher metal concentrations which they lost during ore formation, not recorded in the fluid inclusion assemblage. This explains the notably low concentrations of metals such as Fe, Cu, and Mo in the Dahu solid-free fluid inclusions. These elements typically show enrichment factors of 10–1000 against their crustal averages [87] in magmatic ore fluids (e.g., [9–11, 17, 37, 38]) but are close to or lower than their crustal averages in the Dahu solid-free fluid inclusions.

8.5. Comparison with Orogenic Gold Deposit Fluids.

The Dahu ore fluids marginally overlap with the field of ore fluids of orogenic gold deposits in the K/Na versus Na + K diagrams (Figure 5) and also resemble the ore fluids of orogenic gold deposits in terms of elevated CO_2 contents (i.e., CO_2 presents as one or two separate phases in fluid inclusions at room temperature). The oxidized nature of the Dahu ore fluids, however, is clearly in contrast to the reduced nature of typical orogenic gold deposit fluids. Orogenic gold deposits normally lack oxidized hydrothermal phases such as anhydrite (e.g., [88]) and show elevated concentrations of reduced gases such as CH_4 and N_2 in fluid inclusions (e.g., [24, 25]), while some disputable or atypical orogenic gold deposits with oxidized ore fluids are often suggested to be of magmatic-hydrothermal origin or include significant contributions from magmatic fluids during ore formation, such as the Golden Mile and East Repulse gold deposits in Australia [86, 89, 90], the McIntyre-Hollinger gold deposit in Canada [86], and the Malartic gold deposit in Canada (Helt et al., 2014).

Nevertheless, a comparison to orogenic gold deposits seems unlikely to provide a clear clue for the fluid source of the Dahu deposit. As a specific deposit type, orogenic gold deposits do not share a universal genetic model, with a variety of metamorphic, magmatic, and deep subcrustal models favored by different researchers (e.g., [25] and references therein).

8.6. Possible Fluid Source.

In summary, the stage I and III Dahu ore fluids, despite the apparent differences in Pb, Sr, and Cs concentrations, as well as the abundance of solid phases in fluid inclusions, have similar high K/Na ratio and high Rb concentrations, as well as high oxidation state. These characteristics of the Dahu ore fluids clearly differ from metamorphic fluids but most likely represent two separate pulses of fluids evolved from one (or possibly two) unexposed and oxidized magmatic system (s).

The vein systems of the Dahu deposit, however, must have been emplaced at deeper crustal levels than typically porphyry deposits, which often have an emplacement depth of less than 5 km (e.g., Sillitoe, 1973; Westra et al., 1981). The quartz vein systems at the Dahu deposit were estimated to have formed at 5 to 10 km depth, based on evidence from fluid inclusions and their quartz vein fabric [22]. The large emplacement depth of the Dahu deposit explains the elevated CO_2 contents at the Dahu deposit. The solubility of CO_2 in magma and water generally increases with pressure, and the
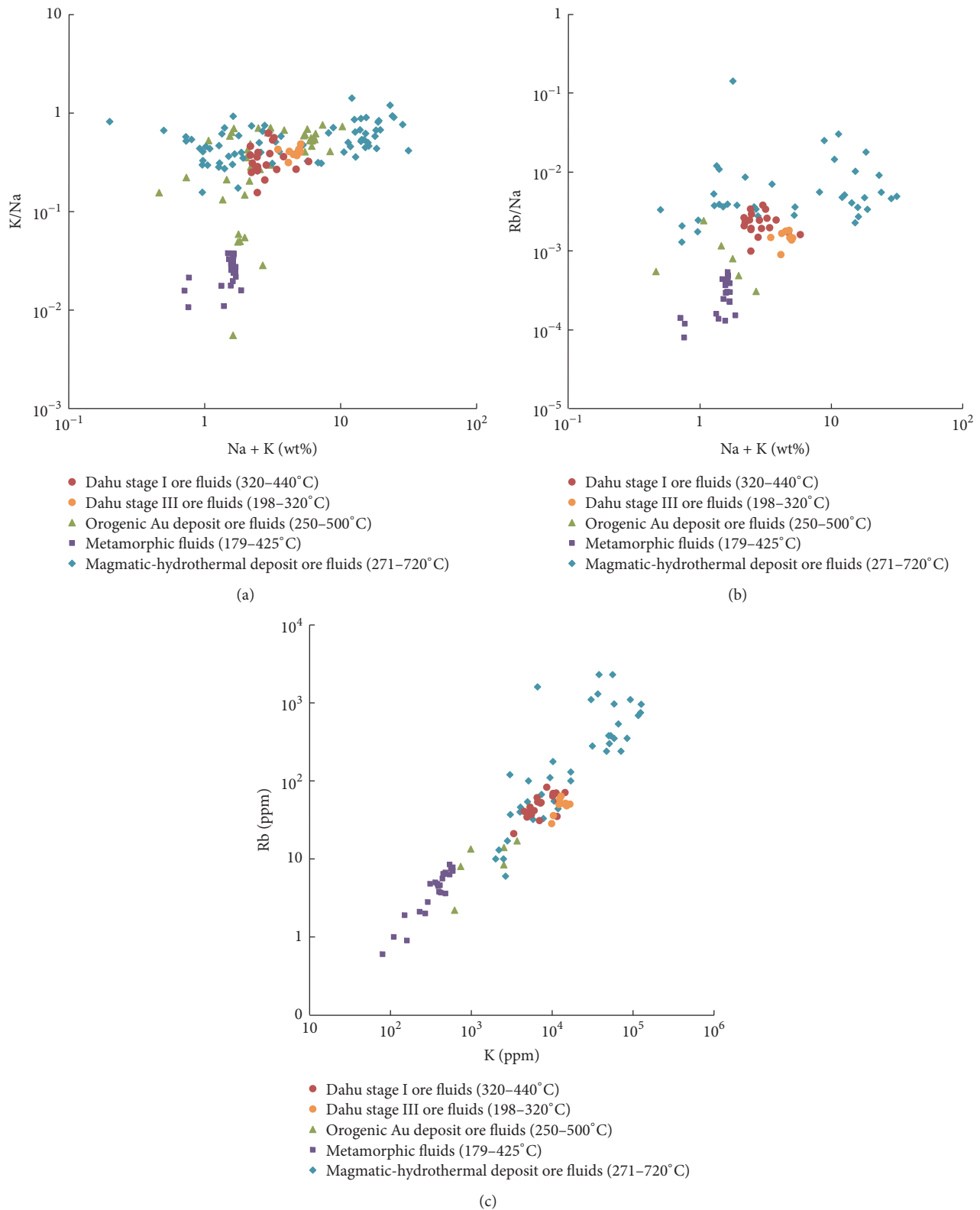
FIGURE 5: Fluid compositions of the Dahu deposit compared to other hydrothermal systems. (a) Fluid compositions plotted in K/Na (weight ratio) versus Na + K space. (b) Fluid compositions plotted in Rb/Na (weight ratio) versus Na + K space. (c) Fluid compositions plotted in Rb versus K space. Estimated trapping temperatures for fluid inclusions are shown in brackets. Data for orogenic Au deposit ore fluids are from Yardley et al. [34], Hodge [29], Garofalo et al. [30], and Morales et al. [31], for metamorphic fluids from Marsala et al. [35] and Miron et al. [36], and for magmatic-hydrothermal deposits (i.e., porphyry and intrusion-related deposits) from Ulrich et al. [9], Rusk et al. [37], Klemm et al. [10, 11], Audétat et al. [38], Seo et al. [12], Stefanova et al. [17], and Catchpole et al. [15].

solubility of CO_2 in magma is generally low relative to that of H_2O; therefore, CO_2-rich fluids tend to form at greater depth (e.g., >10 km or 3 kbar; [24, 91]), although three phase CO_2-H_2O fluids are also known to occur in orogenic gold deposits at much shallower depths (e.g., Diamond 1990).

The greater depth of emplacement also explains the absence of a generative intrusion exposed within the Dahu mining area. At greater depths, intrusions commonly lack proximal zones of high fracture intensity, because the mechanical energy released during crystallization of the intrusions is insufficient to fracture the host rocks in the same way as is proposed for porphyry-related intrusions at shallow crustal levels [92, 93]. Instead, the fluids would be channeled out of the intrusions along intragranular spaces and collected along preexisting fractures which may include those controlling emplacement of the magma, explaining the fault-controlled vein-style mineralization at the Dahu deposit.

A magmatic-hydrothermal origin is also in accordance with the local tectonomagmatic setting of the Dahu deposit. The Late Triassic is a major magmatic period in the Qinling–Dabie orogen, with abundant granitic rocks and mafic dikes emplaced in a postcollisional extensional setting and related to partial melting of the lower crust and an ancient enriched lithospheric mantle beneath the southern margin of the North China craton and the North Qinling Belt. Examples are the Laoniushan granitic complex (228 ± 1–215 ± 4 Ma: [50]) and the Wengyu granite (205 ± 2 Ma: [51]) in the Xiaoqinling region (Figure 1).

A broader implication of this study is that even fluid inclusions showing close spatial associations with the ore mineral of interest may actually represent the spent ore fluids trapped after the precipitation of ore minerals. Therefore, for some ore deposits, perhaps it is necessary to analyze fluid inclusions from the feeder zones beneath to gain a true picture of the initial fertile ore fluid, as suggested by Wilkinson [94].

9. Conclusions

Our investigation demonstrates that UV-fs-LA-ICP-MS analysis of fluid inclusions in a frozen state can improve the analysis of CO_2-rich fluid inclusions by decreasing the internal pressure of fluid inclusions.

The Dahu ore fluids are dominated by Na and K with subordinate amount of B. The low concentrations of Mo (<2 ppm) and other ore components (e.g., Ca, Fe, Cu, Sr, and Mo) in the solid-free stage I fluid inclusions indicate that all analyzed stage I fluid inclusions represent spent ore fluids, trapped after the precipitation of the major ore minerals, in spite of the close spatial association of apparently cogenetic fluid inclusion assemblages and ore minerals.

The Dahu ore fluids clearly differ from metamorphic fluids in compositions, and most likely represent two separate pulses of spent fluids evolved from an unexposed and oxidized magmatic system.

Disclosure

This paper is based on the Ph.D. thesis of Wei Jian [95].

Conflicts of Interest

The authors declare that there are no conflicts of interest regarding the publication of this paper.

Supplementary Materials

Table A1 shows element concentrations in individual solid-bearing fluid inclusions (i.e., composite inclusions or fluid inclusions with accidentally trapped solids) from Dahu stage I quartz. *(Supplementary Materials)*
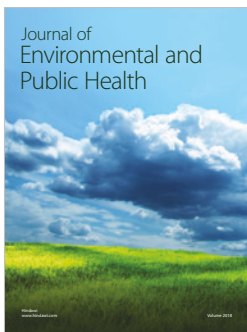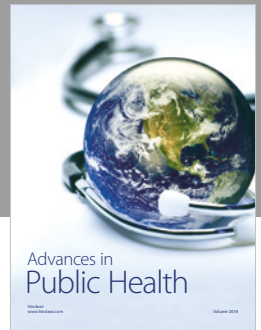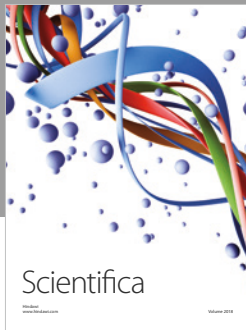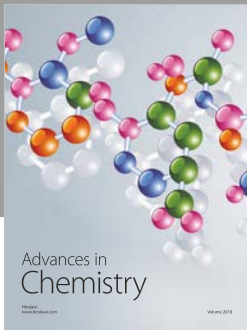
References

[1] D. Günther, A. Audétat, R. Frischknecht, and C. A. Heinrich, "Quantitative analysis of major, minor and trace elements in fluid inclusions using laser ablation-inductively coupled plasma mass spectrometry," *Journal of Analytical Atomic Spectrometry*, vol. 13, no. 4, pp. 263–270, 1998.

[2] C. A. Heinrich, T. Pettke, W. E. Halter et al., "Quantitative multi-element analysis of minerals, fluid and melt inclusions by laser-ablation inductively-coupled-plasma mass-spectrometry," *Geochimica et Cosmochimica Acta*, vol. 67, no. 18, pp. 3473–3496, 2003.

[3] M. M. Allan, B. W. D. Yardley, L. J. Forbes, K. I. Shmulovich, D. A. Banks, and T. J. Shepherd, "Validation of LA-ICP-MS fluid inclusion analysis with synthetic fluid inclusions," *American Mineralogist*, vol. 90, no. 11-12, pp. 1767–1775, 2005.

[4] T. Pettke, F. Oberli, A. Audétat et al., "Recent developments in element concentration and isotope ratio analysis of individual fluid inclusions by laser ablation single and multiple collector ICP-MS," *Ore Geology Reviews*, vol. 44, pp. 10–38, 2012.

[5] A. Audétat, D. Günther, and C. A. Heinrich, "Formation of a magmatic-hydrothermal ore deposit: Insights with LA-ICP- MS analysis of fluid inclusions," *Science*, vol. 279, no. 5359, pp. 2091–2094, 1998.

[6] A. Audétat, "Source and evolution of molybdenum in the porphyry Mo(-Nb) deposit at Cave Peak, Texas," *Journal of Petrology*, vol. 51, no. 8, Article ID egq037, pp. 1739–1760, 2010.

[7] C. A. Heinrich, D. Günther, A. Audétat, T. Ulrich, and R. Frischknecht, "Metal fractionation between magmatic brine and vapor, determined by microanalysis of fluid inclusions," *Geology*, vol. 27, no. 8, pp. 755–758, 1999.

[8] T. Ulrich, D. Günther, and C. A. Heinrich, "Gold concentrations of magmatic brines and the metal budget of porphyry copper deposits," *Nature*, vol. 399, no. 6737, pp. 676–679, 1999.

[9] T. Ulrich, D. Günther, and C. A. Heinrich, "The evolution of a porphyry Cu-Au deposit, based on LA-ICP-MS analysis of

fluid inclusions: Bajo de la Alumbrera, Argentina," *Economic Geology*, vol. 97, no. 8, pp. 1889–1920, 2002.

[10] L. M. Klemm, T. Pettke, C. A. Heinrich, and E. Campos, "Hydrothermal evolution of the El Teniente deposit, Chile: Porphyry Cu-Mo ore deposition from low-salinity magmatic fluids," *Economic Geology*, vol. 102, no. 6, pp. 1021–1045, 2007.

[11] L. M. Klemm, T. Pettke, and C. A. Heinrich, "Fluid and source magma evolution of the questa porphyry Mo deposit, New Mexico, USA," *Mineralium Deposita*, vol. 43, no. 5, pp. 533–552, 2008.

[12] J. H. Seo, M. Guillong, and C. A. Heinrich, "The role of sulfur in the formation of magmatic-hydrothermal copper-gold deposits," *Earth and Planetary Science Letters*, vol. 282, no. 1-4, pp. 323–328, 2009.

[13] C. Pudack, W. E. Halter, C. A. Heinrich, and T. Pettke, "Evolution of magmatic vapor to gold-rich epithermal liquid: The porphyry to epithermal transition at Nevados de Famatina, Northwest Argentina," *Economic Geology*, vol. 104, no. 4, pp. 449–477, 2009.

[14] H. Catchpole, K. Kouzmanov, L. Fontboté, M. Guillong, and C. A. Heinrich, "Fluid evolution in zoned Cordilleran polymetallic veins - Insights from microthermometry and LA-ICP-MS of fluid inclusions," *Chemical Geology*, vol. 281, no. 3-4, pp. 293–304, 2011.

[15] H. Catchpole, K. Kouzmanov, B. Putlitz, J. H. Seo, and L. Fontboté, "Zoned base metal mineralization in a porphyry system: Origin and evolution of mineralizing fluids in the Morococha district, Peru," *Economic Geology*, vol. 110, no. 1, pp. 39–71, 2015.

[16] M. P. Simpson, S. S. Palinkas, J. L. Mauk, and R. J. Bodnar, "Fluid inclusion chemistry of adularia-sericite epithermal Au-Ag deposits of the southern hauraki goldfield, New Zealand," *Economic Geology*, vol. 110, no. 3, pp. 763–786, 2015.

[17] E. Stefanova, T. Driesner, Z. Zajacz, C. A. Heinrich, P. Petrov, and Z. Vasilev, "Melt and fluid inclusions in hydrothermal veins: The magmatic to hydrothermal evolution of the elatsite porphyry Cu-Au deposit, Bulgaria," *Economic Geology*, vol. 109, no. 5, pp. 1359–1381, 2014.

[18] C. Xue, J. Ji, L. Zhang, D. Lu, H. Liu, and Q. Li, "The Jingtieshan submarine exhalative-sedimentary iron-copper deposit in North Qilian mountain," *Mineral Deposits*, vol. 16, no. 1, pp. 151–162, 1997.

[19] H. R. Fan, Y. H. Xie, R. Zhao, and Y. L. Wang, "Dual origins of Xiaoqinling gold-bearing quartz veins: fluid inclusion evidence," *Chinese Science Bulletin*, vol. 45, pp. 1424–1430, 2000.

[20] J. Mao, R. J. Goldfarb, Z. Zhang, W. Xu, Y. Qiu, and J. Deng, "Gold deposits in the Xiaoqinling-Xiong'ershan region, Qinling mountains, central China," *Mineralium Deposita*, vol. 37, no. 3-4, pp. 306–325, 2002.

[21] J.-W. Li, Z.-K. Li, M.-F. Zhou et al., "The early cretaceous Yangzhaiyu lode gold deposit, north China craton: A link between craton reactivation and gold veining," *Economic Geology*, vol. 107, no. 1, pp. 43–79, 2012.

[22] W. Jian, B. Lehmann, J. Mao et al., "Mineralogy, fluid characteristics, and Re-Os age of the late triassic Dahu Au-Mo deposit, Xiaoqinling Region, Central China: Evidence for a magmatic-hydrothermal origin," *Economic Geology*, vol. 110, no. 1, pp. 119–145, 2015.

[23] D. I. Groves, R. J. Goldfarb, M. Gebre-Mariam, S. G. Hagemann, and F. Robert, "Orogenic gold deposits: a proposed classification in the context of their crustal distribution and relationship

to other gold deposit types," *Ore Geology Reviews*, vol. 13, no. 1–5, pp. 7–27, 1998.

[24] J. Ridley, E. Mikucki, and D. Groves, "Archean lode-gold deposits: fluid flow and chemical evolution in vertically extensive hydrothermal systems," *Ore Geology Reviews*, vol. 10, no. 3-6, pp. 279–293, 1996.

[25] R. J. Goldfarb and D. I. Groves, "Orogenic gold: common or evolving fluid and metal sources through time," *Lithos*, vol. 233, pp. 2–26, 2015.

[26] J. R. Lang and T. Baker, "Intrusion-related gold systems: The present level of understanding," *Mineralium Deposita*, vol. 36, no. 6, pp. 477–489, 2001.

[27] T. Baker, "Emplacement depth and carbon dioxide-rich fluid inclusions in intrusion-related gold deposits," *Economic Geology*, vol. 97, no. 5, pp. 1111–1117, 2002.

[28] J. L. Mair, R. J. Goldfarb, C. A. Johnson, C. J. R. Hart, and E. E. Marsh, "Geochemical constraints on the genesis of the Scheelite dome intrusion-related gold deposit, Tombstone gold belt, Yukon, Canada," *Economic Geology*, vol. 101, no. 3, pp. 523–553, 2006.

[29] J. L. Hodge, *Hydrothermal evolution of two stages of gold mineralization at the orogenic new Celebration gold deposit, and implications for gold mineralization within the Kalgoorlie-Kambalda corridor, eastern Goldfields Province, Western Australia*, The University of Western Australia, 2010.

[30] P. S. Garofalo, M. B. Fricker, D. Günther, D. Bersani, and P. P. Lottici, "Physical-chemical properties and metal budget of Au-transporting hydrothermal fluids in orogenic deposits," in *Gold-Transporting Hydrothermal Fluids in the Earth's Crust. The Geological Society of London*, P. S. Garofalo and J. R. Ridley, Eds., vol. 402, pp. 71–102, 2014.

[31] M. J. Morales, R. C. Figueiredo e Silva, L. M. Lobato, S. D. Gomes, C. C. C. O. Gomes, and D. A. Banks, "Metal source and fluid-rock interaction in the Archean BIF-hosted Lamego gold mineralization: Microthermometric and LA-ICP-MS analyses of fluid inclusions in quartz veins, Rio das Velhas greenstone belt, Brazil," *Ore Geology Reviews*, vol. 72, no. 1, pp. 510–531, 2016.

[32] M. Albrecht, I. T. Derrey, I. Horn, S. Schuth, and S. Weyer, "Quantification of trace element contents in frozen fluid inclusions by UV-fs-LA-ICP-MS analysis," *Journal of Analytical Atomic Spectrometry*, vol. 29, no. 6, pp. 1034–1041, 2014.

[33] Z. M. Yang, W. M. Zhang, Y. L. Wu, and etal., "Prospecting report of the Dahu gold deposit, Lingbao County, Henan Province. No. 1 Geological Team, Bureau of Geology and Mineral Resources (BGMR) of Henan Province Internal Report, Luoyang".

[34] B. W. D. Yardley, D. A. Banks, S. H. Bottrell, and L. W. Diamond, "Post-metamorphic gold-quartz veins from NW Italy: the composition and origin of the ore fluid," *Mineralogical Magazine*, vol. 57, no. 3, pp. 407–422, 1993.

[35] A. Marsala, T. Wagner, and M. Wälle, "Late-metamorphic veins record deep ingression of meteoric water: A LA-ICPMS fluid inclusion study from the fold-and-thrust belt of the Rhenish Massif, Germany," *Chemical Geology*, vol. 351, pp. 134–153, 2013.

[36] G. D. Miron, T. Wagner, M. Wälle, and C. A. Heinrich, "Major and trace-element composition and pressure-temperature evolution of rock-buffered fluids in low-grade accretionary-wedge metasediments, Central Alps," *Contributions to Mineralogy and Petrology*, vol. 165, no. 5, pp. 981–1008, 2013.

[37] B. G. Rusk, M. H. Reed, J. H. Dilles, L. M. Klemm, and C. A. Heinrich, "Compositions of magmatic hydrothermal fluids

determined by LA-ICP-MS of fluid inclusions from the porphyry copper-molybdenum deposit at Butte, MT," *Chemical Geology*, vol. 210, no. 1-4, pp. 173–199, 2004.

[38] A. Audétat, T. Pettke, C. A. Heinrich, and R. J. Bodnar, "Special paper: the composition of magmatic-hydrothermal fluids in barren and mineralized intrusions," *Economic Geology*, vol. 103, no. 5, pp. 877–908, 2008.

[39] G. W. Zhang, B. R. Zhang, X. C. Yuan, and Q. H. Xiao, *Qinling orogenic belt and continental dynamics*, Science Press, Beijing, China, 2001.

[40] Y. Dong, G. Zhang, F. Neubauer, X. Liu, J. Genser, and C. Hauzenberger, "Tectonic evolution of the Qinling orogen, China: review and synthesis," *Journal of Asian Earth Sciences*, vol. 41, no. 3, pp. 213–237, 2011.

[41] J. W. Mao, G. Q. Xie, F. Bierlein et al., "Tectonic implications from Re-Os dating of Mesozoic molybdenum deposits in the East Qinling-Dabie orogenic belt," *Geochimica et Cosmochimica Acta*, vol. 72, no. 18, pp. 4607–4626, 2008.

[42] N. Z. Cai and Z. B. Su, "Stratigraphic subdiision and distinction of primary rock-types of the taihua group in the Xiaoqinling Mountain," *Regional Geology of China*, vol. 13, pp. 35–44, 1985.

[43] H. W. Zhou, Z. Q. Zhong, W. L. Ling, G. L. Zhong, and Q. D. Xu, "Sm-Nd isochron for the amphibolites within Taihua complex from Xiao Qinling area, Western Henan and its geological implications," *Geochimica et Cosmochimica Acta*, vol. 27, Article ID 367372, pp. 367–372, 1998.

[44] Z. Y. Ni, R. M. Wang, Y. Tong, C. Yang, and T. M. Dai, "^{207}Pb/^{206}Pb Age of zircon and ^{40}Ar/^{39}Ar of amphibole from plagioclase amphibolite in the Taihua Group, Luoning, Henan, China," *Geological Review*, vol. 49, Article ID 361366, pp. 361–366, 2003.

[45] H. M. Li, Y. C. Chen, D. H. Wang et al., "SHRIMP U-Pb ages of metamorphic rocks and veins in the Xiaoqinling area, and their geological significance," *Acta Petrologica Sinica*, vol. 23, pp. 2504–2512, 2007.

[46] S. M. Li, L. Q. Qu, Z. B. Su, J. J. Huang, X. S. Wang, and Z. S. Yue, *The geology and metallogenic prediction of the gold deposit in Xiaoqinling*, Geological Publishing House, Beijing, China, 1996.

[47] T. Wang, J. Mao, and Y. Wang, "Research on SHRIMP U-Pb chronology in Xiaoqinling-Xionger' shan area: The evidence of delamination of lithosphere in Qinling orogenic belt," *Acta Petrologica Sinica*, vol. 24, no. 6, pp. 1273–1287, 2008.

[48] H. J. Zhao, J. W. Mao, H. S. Ye, G. Q. Xie, and Z. X. Yang, "Geochronology and geochemistry of the alkaline granite porphyry and diabase dikes in Huanglongpu area of Shanxi Province: Petrogenesis and implications for tectonic environment," *Geology in China*, vol. 37, pp. 12–27, 2010.

[49] S. J. Bi, J. W. Li, and Z. K. Li, "a. Geological significance and geochronology of Paleproterozoic mafic dykes of Xiaoqinling gold district, southern margin of the North China Craton," *Earth Science—Journal of China University of Geosciences*, vol. 36, pp. 17–32, 2011.

[50] L.-X. Ding, C.-Q. Ma, J.-W. Li et al., "Timing and genesis of the adakitic and shoshonitic intrusions in the Laoniushan complex, southern margin of the North China Craton: Implications for post-collisional magmatism associated with the Qinling Orogen," *Lithos*, vol. 126, no. 3-4, pp. 212–232, 2011.

[51] J. Hu, S.-Y. Jiang, H.-X. Zhao et al., "Geochemistry and petrogenesis of the Huashan granites and their implications for Mesozoic tectonic settings in the Xiaoqinling gold mineralization belt, NW China," *Journal of Asian Earth Sciences*, vol. 56, pp. 276–289, 2012.

[52] J.-W. Mao, G.-Q. Xie, F. Pirajno et al., "Late jurassic-early cretaceous granitoid magmatism in eastern qinling, central-eastern china: Shrimp zircon u-pb ages and tectonic implications," *Australian Journal of Earth Sciences*, vol. 57, no. 1, pp. 51–78, 2010.

[53] Y. T. Wang, H. S. Ye, A. W. Ye, Y. Sun, Y. G. Li, and C. Q. Zhang, "Zircon SHRIM P U-Pb ages and their significances of the Wenyu and Niangniangshan granitic plutons in the Xiaoqinling area, central China," *Chinese Journal of Geology*, vol. 45, Article ID 167180, pp. 167–180, 2010.

[54] X. X. Wang, T. Wang, Q. J. Qi, and S. Li, "Temporal-spatial variations, origin and their tectonic significance of the Late Mesozoic granites in the Qinling, Central China," *Acta Petrologica Sinica*, vol. 27, Article ID 15731593, pp. 1573–1593, 2011.

[55] J.-W. Li, S.-J. Bi, D. Selby et al., "Giant Mesozoic gold provinces related to the destruction of the North China craton," *Earth and Planetary Science Letters*, vol. 349-350, pp. 26–37, 2012.

[56] H.-X. Zhao, S.-Y. Jiang, H. E. Frimmel, B.-Z. Dai, and L. Ma, "Geochemistry, geochronology and Sr-Nd-Hf isotopes of two Mesozoic granitoids in the Xiaoqinling gold district: Implication for large-scale lithospheric thinning in the North China Craton," *Chemical Geology*, vol. 294-295, pp. 173–189, 2012.

[57] S.-J. Bi, J.-W. Li, M.-F. Zhou, and Z.-K. Li, "Gold distribution in As-deficient pyrite and telluride mineralogy of the Yangzhaiyu gold deposit, Xiaoqinling district, southern North China craton," *Mineralium Deposita*, vol. 46, no. 8, pp. 925–941, 2011.

[58] W. Jian, B. Lehmann, J. Mao et al., "Telluride and Bi-sulfosalt mineralogy of the Yangzhaiyu gold deposit, Xiaoqinling region, Central China," *The Canadian Mineralogist*, vol. 52, no. 5, pp. 883–898, 2014.

[59] N. Li, Y. L. Sun, J. Li, L. W. Xue, and W. B. Li, "Molybdenite Re-Os isotope age of the Dahu Au-Mo deposit, Xiaoqinling and the Indosinian mineralization," *Acta Petrologica Sinica*, vol. 24, no. 4, pp. 810–816, 2008.

[60] N. Li, Y.-J. Chen, I. R. Fletcher, and Q.-T. Zeng, "Triassic mineralization with cretaceous overprint in the dahu au-mo deposit, xiaoqinling gold province: Constraints from shrimp monazite u-th-pb geochronology," *Gondwana Research*, vol. 20, no. 2-3, pp. 543–552, 2011.

[61] Z. Y. Ni, N. Li, S. J. Guan, H. Zhang, and L. W. Xue, "Characteristics of fluid inclusions and ore genesis of the Dahu Au-Mo deposit in the Xiaoqinling gold field, Henan province," *Acta Petrologica Sinica*, vol. 24, no. 9, pp. 2058–2068, 2008.

[62] Z.-Y. Ni, Y.-J. Chen, N. Li, and H. Zhang, "Pb-Sr-Nd isotope constraints on the fluid source of the Dahu Au-Mo deposit in Qinling Orogen, central China, and implication for Triassic tectonic setting," *Ore Geology Reviews*, vol. 46, pp. 60–67, 2012.

[63] Y.-H. Zhang, J.-W. Mao, M.-X. Yu, and Z.-Y. Li, "Mo-bearing quartz vein by acid leaching: Evidences from Dahu-Qinnan mine in northern belt of Xiaoqinling gold province, Central China," *Journal of Jilin University (Earth Science Edition)*, vol. 42, no. 4, pp. 1011–1025, 2012.

[64] J. Z. Feng, X. C. Wang, W. Z. Sun et al., "Prospecting report of the Dahu gold deposit, Lingbao County, Henan Province. Luoyang, No. 1 Geological Team of BGMR of Henan province".

[65] E. Roedder, "Fluid inclusions," *Reviews in Mineralogy and Geochemistry*, pp. 1–644, 1984.

[66] P. L. F. Collins, "Gas hydrates in CO_2-bearing fluid inclusions and the use of freezing data for estimation of salinity," *Economic Geology*, vol. 74, no. 6, pp. 1435–1444, 1979.

[67] M. Guillong, D. L. Meier, M. M. Allan, C. A. Heinrich, and B. W. D. Yardley, "SILLS: A Matlab-based program for the

reduction of laser ablation ICP-MS data of homogeneous material and inclusions," in *Laser ablation ICP–MS in the earth sciences: current practices and outstanding issues, Mineralogical Association of Canada Short Course 40 volume. Mineralogical Association of Canada*, P. Sylvester, Ed., pp. 328–333, Vancouver, Canada, 2008.

[68] I. Horn, F. Von Blanckenburg, R. Schoenberg, G. Steinhoefel, and G. Markl, "In situ iron isotope ratio determination using UV-femtosecond laser ablation with application to hydrothermal ore formation processes," *Geochimica et Cosmochimica Acta*, vol. 70, no. 14, pp. 3677–3688, 2006.

[69] I. Horn and F. Von Blanckenburg, "Investigation on elemental and isotopic fractionation during 196 nm femtosecond laser ablation multiple collector inductively coupled plasma mass spectrometry," *Spectrochimica Acta Part B: Atomic Spectroscopy*, vol. 62, no. 4, pp. 410–422, 2007.

[70] G. Steinhoefel, I. Horn, and F. Von Blanckenburg, "Matrix-independent Fe isotope ratio determination in silicates using UV femtosecond laser ablation," *Chemical Geology*, vol. 268, no. 1-2, pp. 67–73, 2009.

[71] M. Lazarov and I. Horn, "Matrix and energy effects during in-situ determination of Cu isotope ratios by ultraviolet-femtosecond laser ablation multicollector inductively coupled plasma mass spectrometry," *Spectrochimica Acta Part B: Atomic Spectroscopy*, vol. 111, pp. 64–73, 2015.

[72] T. Pettke, "Analytical protocols for element concentration and isotope ratio measurements in fluid inclusions by LA-(MC)-ICP-MS," in *Laser Ablation ICP-MS in the Earth Sciences: Current Practices And Outstanding Issues: Mineralogical Association of Canada Short Course*, P. Sylvester, Ed., vol. 40, pp. 189–218, Mineralogical Association of Canada, Vancouver, Canada, 2008.

[73] L. Klemm, T. Pettke, S. Graeser, J. Mullis, and K. Kouzmanov, "Fluid mixing as the cause of sulphide precipitation at Albrunpass, Binn Valley, Central Alps," *Schweizerische mineralogische und petrographische Mitteilungen*, vol. 84, no. 1-2, pp. 189–212, 2004.

[74] R. H. Sibson and J. Scott, "Stress/fault controls on the containment and release of overpressured fluids: examples from gold-quartz vein systems in Juneau, Alaska; Victoria, Australia and Otago, New Zealand," *Ore Geology Reviews*, vol. 13, no. 1-5, pp. 293–306, 1998.

[75] S. F. Simmons and K. L. Brown, "Gold in magmatic hydrothermal solutions and the rapid formation of a giant ore deposit," *Science*, vol. 314, no. 5797, pp. 288–291, 2006.

[76] B. W. D. Yardley and R. J. Bodnar, "Fluids in the Continental Crust," *Geochemical Perspectives*, vol. 3, no. 1, pp. 20–38, 2014.

[77] R. O. Fournier and A. H. Truesdell, "An empirical NaKCa geothermometer for natural waters," *Geochimica et Cosmochimica Acta*, vol. 37, no. 5, pp. 1255–1275, 1973.

[78] B. Luckscheiter and G. Morteani, "Microthermometrical and chemical studies of fluid inclusions in minerals from Alpine veins from the penninic rocks of the central and western Tauern Window (Austria/Italy)," *Lithos*, vol. 13, no. 1, pp. 61–77, 1980.

[79] G. Bozkaya, D. A. Banks, F. Ozbas, and J. Wallington, "Fluid processes in the Tesbihdere base-metal-Au deposit: Implications for epithermal mineralization in the Biga Peninsula, NW Turkey," *Central European Journal of Geosciences*, vol. 6, no. 2, pp. 148–169, 2014.

[80] S. E. Kesler, "Ore-Forming Fluids," *Elements*, vol. 1, no. 1, pp. 13–18, 2005.

[81] K. S. Heier and J. A. S. Adams, "The geochemistry of the alkali metals," *Physics and Chemistry of the Earth*, vol. 5, no. C, pp. 253–381, 1964.

[82] S. Ishihara, "The granitoid series and mineralization," *Economic Geology, Seventy-fifth Anniversary Volume (1905-1980)*, pp. 458–484, 1981.

[83] R. H. Sillitoe and J. F. H. Thompson, "Intrusion-related vein gold deposits: types, tectono-magmatic settings and difficulties of distinction from orogenic gold deposits," *Resource Geology*, vol. 48, no. 4, pp. 237–250, 1998.

[84] R. H. Sillitoe, "Porphyry copper systems," *Economic Geology*, vol. 105, no. 1, pp. 3–41, 2010.

[85] B. Lehmann, *Metallogeny of tin*, Springer, Berlin, Germany, 1990.

[86] E. M. Cameron and K. Hattori, "Archean gold mineralization and oxidized hydrothermal fluids.," *Economic Geology*, vol. 82, no. 5, pp. 1177–1191, 1987.

[87] R. L. Rudnick and S. Gao, "Composition of the continental crust," in *The Crust, Treatise in Geochemistry*, R. L. Rudnick, Ed., vol. 3-9, pp. 1–64, 2003.

[88] R. J. Goldfarb, T. Baker, B. Dubé, D. I. Groves, C. J. R. Hart, and P. Gosselin, "Distribution, character, and genesis of gold deposits in metamorphic terranes," *Economic Geology 100th Anniversary Volume*, pp. 407–450, 2005.

[89] A. G. Mueller, "Copper-gold endoskarns and high-Mg monzodiorite-tonalite intrusions at Mt. Shea, Kalgoorlie, Australia: Implications for the origin of gold-pyrite-tennantite mineralization in the Golden Mile," *Mineralium Deposita*, vol. 42, no. 7, pp. 737–769, 2007.

[90] A. B. Bath, J. L. Walshe, J. Cloutier et al., "Biotite and apatite as tools for tracking pathways of oxidized fluids in the archean east repulse gold deposit, Australia," *Economic Geology*, vol. 108, no. 4, pp. 667–690, 2013.

[91] J. B. Lowenstern, "Carbon dioxide in magmas and implications for hydrothermal systems," *Mineralium Deposita*, vol. 36, no. 6, pp. 490–502, 2001.

[92] C. W. Burnham and H. Ohmoto, "Late stage processes in felsic magmatism," in *Mining Geology Special Issue 8. Society of mining geologists of Japan*, S. Ishihara and S. Takenouchi, Eds., pp. 1–12, 1980.

[93] P. J. Pollard, "An intrusion-related origin for Cu-Au mineralization in iron oxide-copper-gold (IOCG) provinces," *Mineralium Deposita*, vol. 41, no. 2, pp. 179–187, 2006.

[94] J. J. Wilkinson, "Fluid inclusions in hydrothermal ore deposits," *Lithos*, vol. 55, no. 1-4, pp. 229–272, 2001.

[95] W. Jian, *Gold and molybdenum metallogeny in the Xiaoqinling region of central China*, Technische Universität Clausthal, 2015.